Vol 18 No 7, July 2009
1674-1056/2009/18(07)/3066-07

Chinese Physics B

© 2009 Chin. Phys. Soc.
and IOP Publishing Ltd

An effective scatter correction method based on single scatter simulation for a 3D whole-body PET scanner*

Gao Fei(高 飞)[a], Yamada Ryoko[b], Watanabe Mitsuo[b], and Liu Hua-Feng(刘华锋)[a]

[a] *State Key Laboratory of Modern Optical Instrumentation, Zhejiang University, Hangzhou* 310027, *China*

[b] *Central Research Laboratory, Hamamatsu Photonics K.K., Hamamatsu* 434-8601, *Japan*

(Received 24 November 2008; revised manuscript received 12 January 2009)

Hamamatsu SHR74000 is a newly designed full three-dimensional (3D) whole body positron emission tomography (PET) scanner with small crystal size and large field of view (FOV). With the improvement of sensitivity, the scatter events increase significantly at the same time, especially for large objects. Monte Carlo simulations help us to understand the scatter phenomena and provide good references for scatter correction. In this paper, we introduce an effective scatter correction method based on single scatter simulation for the new PET scanner, which accounts for the full 3D scatter correction. With the results from Monte Carlo simulations, we implement a new scale method with special concentration on scatter events from outside the axial FOV and multiple scatter events. The effects of scatter correction are investigated and evaluated by phantom experiments; the results show good improvements in quantitative accuracy and contrast of the images, even for large objects.

Keywords: positron emission tomography, scatter correction, single scatter simulation, Monte Carlo

PACC: 7870

1. Introduction

Positron emission tomography (PET) imaging relies on the coincident detection of positron annihilation photons. In fully three-dimensional (3D) PET imaging, the allowance of acquisition of all the oblique planes increases the sensitivity, while scatter events increase significantly compared with those in 2D PET imaging with inter-slice septa. Therefore, scatter correction is necessary for quantitative accuracy in full 3D PET volume imaging.

The single scatter simulation (SSS) algorithm was first introduced by Ollinger[1] and Watson,[2,3] and many efforts have been made to improve the efficiency of SSS based scatter correction methods.[4,5] The basic idea of single scatter simulation is to calculate the scatter distribution associated with an activity and scatter medium distribution. With the development of PET scanners having a large field of view (FOV), the influence of scatter events is becoming more serious, especially for large objects.

The aim of this work is to develop a new, effective scatter correction code based on the SSS algorithm for the 3D whole-body PET scanner. Monte Carlo simulations are by far the best tool to study the photon interactions in the scatter medium.[6−9] With the help of Monte Carlo simulations, a new scaling method with special concentration on scatter events from outside the axial FOV and multiple scatter events[10,11] has been studied; this makes the scatter correction more effective. Experiments are performed based on the new full 3D whole-body PET/CT scanner: SHR74000 designed by Hamamatsu Photonics K.K., and the effects of scatter correction are investigated and evaluated in this paper.

2. Scanner and Methods

2.1. PET scanner

The full 3D whole body PET scanner SHR74000 designed by Hamamatsu Photonics K.K. is shown in Fig.1. The PET scanner is designed with 6 rings of 48 detector blocks. Each detector block consists of a 16 × 16 array of lutetium yttrium orthosilicate (LYSO) crystals. Each LYSO crystal is 2.9 mm × 2.9 mm ×

*Project supported by the National Natural Science Foundation of China (Grant No 60772125), the Key Foundation of Guangdong Province of China (Grant No 07117784), and Scientific Plan of Zhejiang Province of China (Grant No 2008C23060).

†Corresponding author. E-mail: gaof@zju.edu.cn

20 mm. The ring diameter of the scanner is 826 mm. The scanner has a large FOV: the transaxial FOV is 576 mm, and the axial FOV is 318 mm. Two 30 mm thick side-shieldings are placed on the each side of the scanner; the inner radius of the side-shielding is 375 mm. The main specifications of the scanner are listed in Table 1. The energy window is set to be 400 keV–650 keV during acquisition. Results from Monte Carlo simulations for performance evaluation demonstrate that the scatter fraction of the full 3D whole-body PET scanner SHR74000 is around 40%–60%, and the multiple scatter events comprise 20%–40% of the total scatter events. Here we concentration on large objects.



Fig.1. SHR74000 PET scanner.

Table 1. SHR74000 main specifications.

crystal material	LYSO
crystal size	2.9 mm × 2.9 mm × 20 mm
crystal array on the PMT	256 (16×16/PMT)
PMT type	Hamamatsu R8400
number of crystals	73 728
number of PMTs	288
number of rings	96
ring diameter	826 mm
transaxial FOV	576 mm
axial FOV	318 mm

2.2. Single scatter approximation

The expected single scatter approximation due to scatter in the object can be written as[2]

$$S^{\mathrm{AB}} = \int_V \mathrm{d}V \left(\frac{\sigma_{\mathrm{AS}}\sigma_{\mathrm{BS}}}{4\pi R_{\mathrm{AS}}^2 R_{\mathrm{BS}}^2} \right) \frac{\mu}{\sigma_{\mathrm{c}}} \frac{\mathrm{d}\sigma_{\mathrm{c}}}{\mathrm{d}\Omega} [I_{\mathrm{A}} + I_{\mathrm{B}}], \quad (1)$$

where

$$I_{\mathrm{A}} = \epsilon_{\mathrm{AS}}(E)\epsilon_{\mathrm{BS}}(E') \mathrm{e}^{-\int_S^{\mathrm{A}} \mu(E,x)\mathrm{d}s} \mathrm{e}^{-\int_S^{\mathrm{B}} \mu(E',x)\mathrm{d}s} \times \int_S^{\mathrm{A}} \lambda \mathrm{d}s,$$

$$I_{\mathrm{B}} = \epsilon_{\mathrm{AS}}(E')\epsilon_{\mathrm{BS}}(E) \mathrm{e}^{-\int_S^{\mathrm{A}} \mu(E',x)\mathrm{d}s} \mathrm{e}^{-\int_S^{\mathrm{B}} \mu(E,x)\mathrm{d}s} \times \int_S^{\mathrm{B}} \lambda \mathrm{d}s,$$

where V is the sampled scatter volume, S is the scatter point, A and B are sampled detectors, so S^{AB} is the coincidence scatter rate in detectors A and B, σ_{AS} and σ_{BS} are the detector cross sections presented to the rays AS and BS, R_{AS} and R_{BS} are the distances from S to A and B. σ_{c} and $\mathrm{d}\sigma_{\mathrm{c}}$ are the total and differential Compton scattering cross sections, Ω is the solid angle, E is the energy of the non-scattered photon, E' is the energy of the scattered photon, $\epsilon_{\mathrm{AS}}(E)$ and $\epsilon_{\mathrm{BS}}(E)$ are the approximated detector efficiencies for gamma rays which are incident along AS and BS, $\mu(E,x)$ is the linear attenuation coefficient at the energy E and position x, and λ is the estimated activity distribution from reconstructed images.

2.3. Data processing

The whole procedure of scatter correction based on SSS is shown in Fig.2. With the pre-reconstructed emission images and transmission images, the SSS calculation is performed, and full 3D scatter sinograms were obtained. Using the scale factors mentioned in the next section, we scale and subtract the scatter sinograms from the acquired emission sinograms, then the scatter-corrected sinograms are reconstructed to get the scatter-corrected emission images.

2.4. Scale factor

As in the procedure shown in the previous section, after the single scatter events are estimated, they need to be scaled to the measured emission data before subtraction. The scale step determines the quantitative accuracy of the scatter correction method. Since SSS only calculates the single scatter events inside the axial FOV, they must be scaled to meet the effects of scatter events from outside the axial FOV and multiple scatter events, and here we give special concentration on large objects, in which multiple scatter events

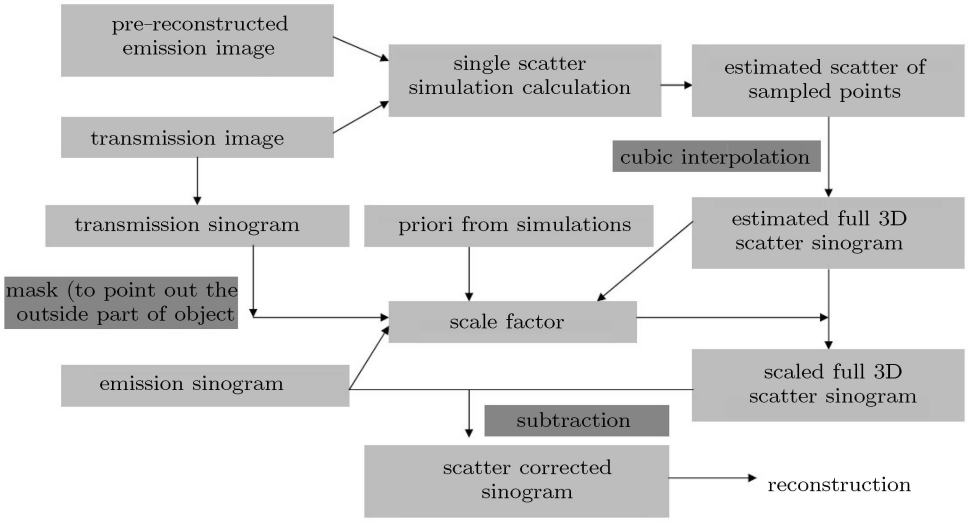


Fig.2. The procedure of scatter correction based on SSS.

increase significantly. In order to treat these two kinds of scatter events explicitly, a new scale factor $f_{\text{scale}}(n,m)$ for every slice can be expressed as

$$f_{\text{scale}}(n,m) = (An^2+Bn+\text{offset})(1+Cm+D)F. \quad (2)$$

Here, n is the axial position, and m is the cross-sectional area of the object in the slice. F is the scatter correction factor through all slices used in the traditional SSS scatter correction method, and it is calculated from tail-fitting in the scatter-only area (outside the object); the effect of F is to compensate the error in approximation of the coincidence detection efficiency. In our method, two additional coefficients $(An^2+Bn+\text{offset})$ and $(1+Cm+D)$ are incorporated for correcting scatter events from outside the axial FOV and multiple scatter events. $(An^2+Bn+\text{offset})$ is the factor related to the axial position to represent the differences in axial sensitivity caused by the influence of activities from outside the axial FOV. The factor $(1+Cm+D)$ is related to the object cross-sectional area to represent variances of multiple scatter events. How the two factors arise is described as follows.

For scatter events from outside the axial FOV, Monte Carlo simulations demonstrate that they occupy about 11% of the total scatter events acquired. Two set of simulations were performed with cylindrical phantoms of different lengths for comparison (one is 318 mm, equal to the axial FOV of the scanner, the other is 700 mm, equal to the NEMA standard); the activity concentration per unit volume was set to be the same. The diameter of one phantom was large (35 cm) and one normal (20 cm), and both phantoms were positioned in the centre of the transaxial FOV during acquisition. To some extent, they can be treated as simulations of the thorax and the head respectively. The results of the axial counts distribution with and without contamination from outside the axial FOV are shown in Figs.3 and 4.

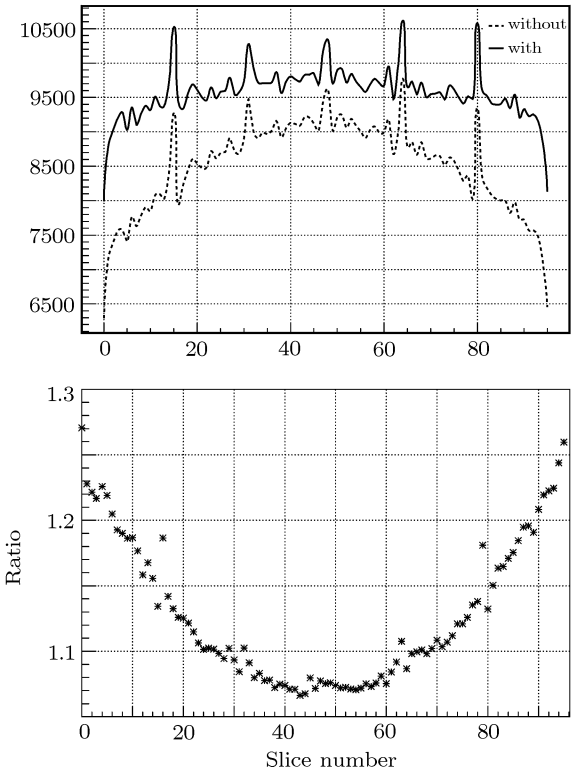


Fig.3. Axial counts distribution with and without contamination from outside the axial FOV for the 35 cm diameter phantom. The top one is the counts varied from slices, the bottom one is the ratio.

The five abnormal peak values in the figures come from the gaps between detector blocks in the newly de-

signed PS-PMT by Hamamatsu. The ratios of counts with and without scatter events from outside the axial FOV are calculated. According to the ratio profiles, a quadratic curve fitting is easy to obtain. The factor $(An^2+Bn+\text{offset})$ for scatter events from outside the axial FOV makes use of these quadratic fitting results. The central slice was set as $n=0$, and both sides were calculated. For the 35 cm diameter phantom, the values of A, B and offset used in practice were 1.13×10^{-4}, -5.87×10^{-4} and 1.063 respectively; for the 20 cm diameter phantom, the values of A, B and offset were 3.05×10^{-5}, 2.39×10^{-3} and 1.072 respectively.

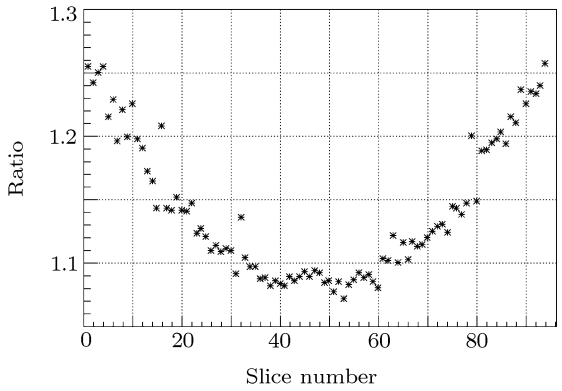


Fig.4. Axial count ratios with and without contamination from outside the axial FOV for the 20 cm diameter phantom.

Monte Carlo simulations demonstrate that multiple scatter events occupy 20%–40% of the total scatter events. We designed a series of simulations by phantoms with elliptic cross sections to find the relationship between the multiple scatter events and object sizes; the dimensions of every elliptic cross section are listed in Table 2. The length of each phantom is 318 mm; all phantoms were positioned in the centre of the transaxial FOV during simulations. The percentages of multiple scatter events to total scatter events are also listed in Table 2. The fitted relationship according to Table 2 is shown in Fig.5: an approximate linear relationship can be obtained directly. The factor $(1+Cm+D)$ for multiple scatter events makes use of these linear fitting results.

Table 2. Simulation record with different elliptic phantoms. 'Percentage' is the ratio of multiple scatter events to total scatter events. 'Object size' is the transverse cross-sectional area of the phantom.

semimajor	semiminor	percentage	object size/mm^2
175	170	29.959%	29 750 π
175	160	29.304%	28 000 π
175	150	28.648%	26 250 π
175	125	26.548%	21 875 π
175	100	23.773%	17 500 π
140	100	22.606%	14 000 π
130	100	22.113%	13 000 π
120	100	21.671%	12 000 π
105	100	20.632%	10 500 π

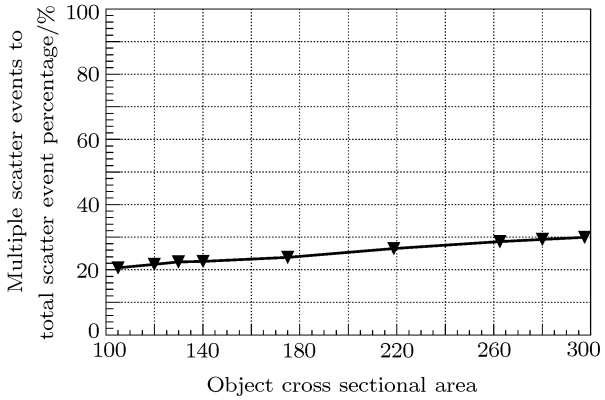


Fig.5. The fitted relationship between multiple scatter events and object cross-sectional area (unit: 100π mm^2).

3. Phantom experiments and results

To evaluate the effects of the proposed scatter correction method, experiments with two cylindrical phantoms were performed. The transverse views are shown in Fig.6. The phantoms are called 'Phantom A' (the left one in Fig.6) and 'Phantom B' (the right one in Fig.6) in the following parts. Here, Monte Carlo simulation code Gean4 Application Tomographic Emission (GATE)[8] was used to produce data for validation of the correction accuracy.

Phantom A: a 350 mm diameter, 700 mm long, water-filled cylindrical phantom, within which two 50 mm diameter, 700 mm long small cylinders were inserted. The two small cylinders were filled with F-18 solutions of the same amount. The aim of this experiment was to test the effect of scatter correction in the transverse central area of the large diameter phantom A. The images were reconstructed using the EM algorithm with and without scatter correction. Fig.7 shows the profiles of the reconstructed images along the dotted line shown in Fig.7; the images were sums of 25 slices (slice 13–37) to improve statistical expression. The results show improvements in contrast. The slight over-estimation in the central area can be calibrated by transmission images from a CT scan.

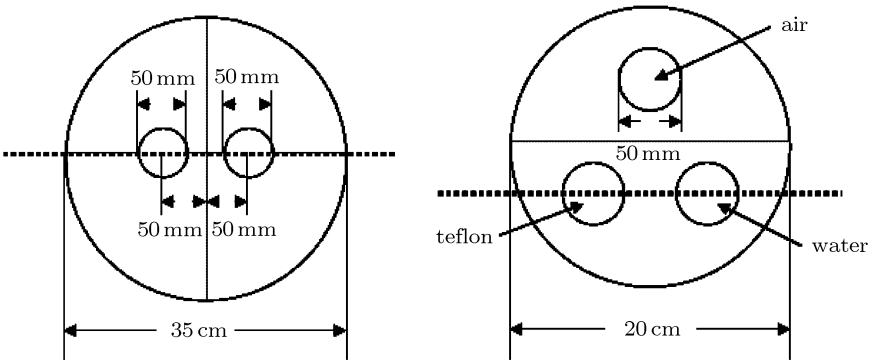


Fig.6. The transverse view of phantom A (left) and phantom B (right).

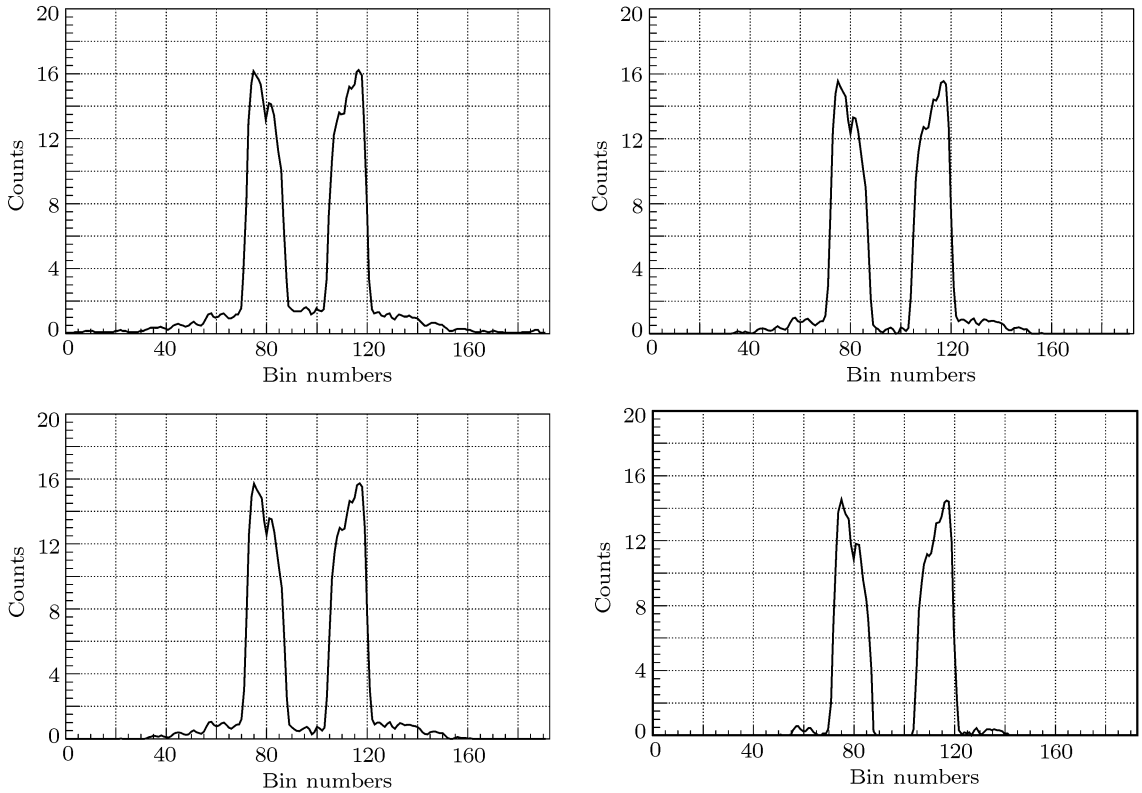


Fig.7. The profiles of reconstructed images of phantom A without scatter correction and with scatter corrections using different scale factors. From top to bottom: 1st: the profile without scatter correction; 2nd: the profile with scatter correction using a common scale factor from tail fitting; 3rd: the profile with scatter correction using a scale factor with correction for scatter events from outside the axial FOV incorporated; 4th: the profile with scatter correction using a scale factor with correction for scatter events from outside the axial FOV and multiple scatter events incorporated.

Phantom B: the attenuation and scatter correction phantom. It is a 200 mm diameter, 700 mm long, water-filled cylindrical phantom. Three small cylinders were inserted. The materials were 'air', 'water' and 'Teflon' respectively; detailed positions and sizes are shown in Fig.6. The big cylinder was filled with F-18 solutions. The aim of this experiment was to test the effects of the new scale method on a standard phantom. The images were reconstructed by using the DRAMA algorithm with attenuation correction. Figure 8 shows the profiles of the reconstructed images along the dotted line shown in Fig.6. In order to reflect the influence of the scatter events from outside the axial FOV more obviously, Fig.8 shows profiles of the 15th slice from the edge of the FOV. The improvements are observed through comparison among scatter corrections with different scale methods, especially in activity-free regions.

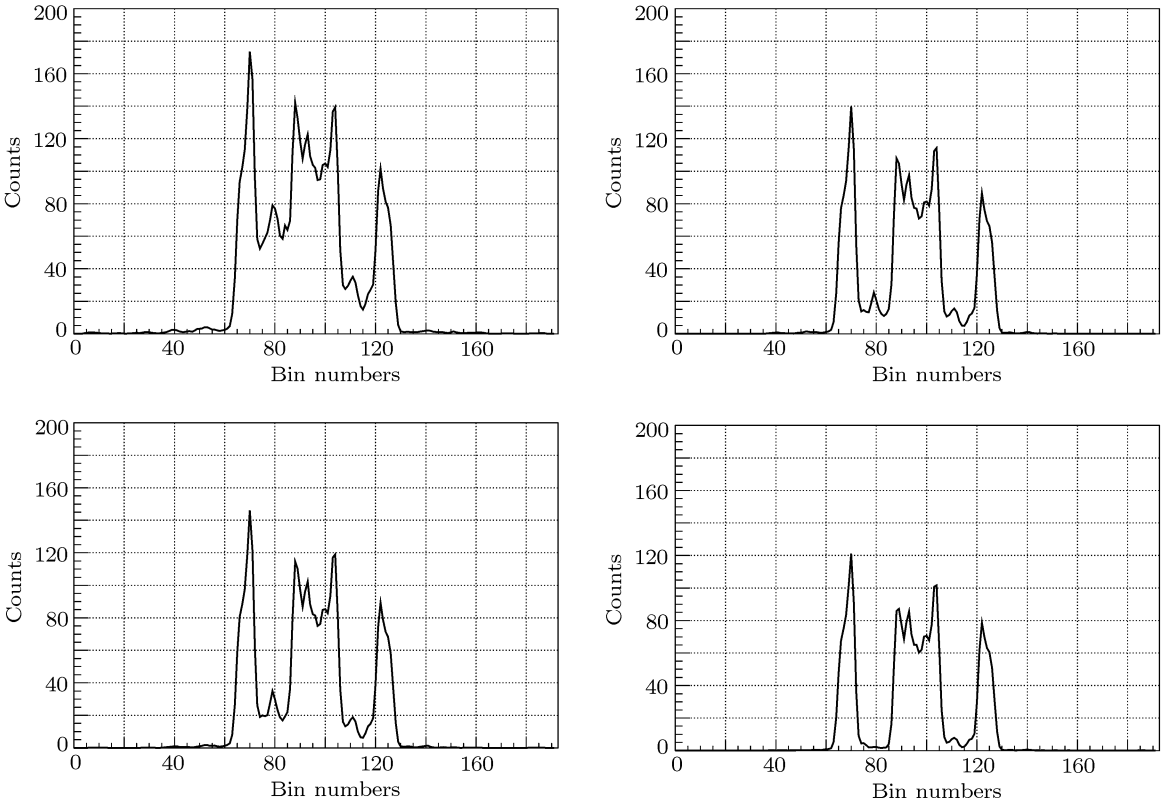


Fig.8. The profiles of reconstructed images of phantom B without scatter correction and with scatter corrections using different scale factors. From top to bottom: 1st: the profile without scatter correction; 2nd: the profile with scatter correction using a common scale factor from tail fitting; 3rd: the profile with scatter correction using a scale factor with correction for scatter events from outside the axial FOV incorporated; 4th: the profile with scatter correction using a scale factor with correction for scatter events from outside the axial FOV and multiple scatter events incorporated.

A statistical analysis on the scatter-corrected results against true values in both activity-free regions and hot regions is performed. Let N_{p} be the total number of pixels and $\hat{x_i}$ be the final reconstruction result of pixel i after scatter correction, and XT_i be the true value of pixel i through all the regions of interest, then we have the following error definitions. For activity-free regions

$$\mathrm{bias} = \frac{1}{N_{\mathrm{p}}} \sum_i (\hat{x_i} - XT_i), \tag{3}$$

$$\mathrm{std} = \left(\frac{1}{N_{\mathrm{p}} - 1} \sum_i (\hat{x_i} - XT_i)^2 \right)^{0.5}. \tag{4}$$

For hot regions

$$\mathrm{bias} = \frac{1}{N_{\mathrm{p}}} \sum_i \frac{\hat{x_i} - XT_i}{XT_i}, \tag{5}$$

$$\mathrm{std} = \left(\frac{1}{N_{\mathrm{p}} - 1} \sum_i \left(\frac{\hat{x_i} - XT_i}{XT_i} \right)^2 \right)^{0.5}. \tag{6}$$

The calculated bias and standard derivation values of the results from different scatter correction methods are summarized in Table 3 (for phantom A) and Table 4 (for phantom B). The quantitative analysis shows the improvements of the bias and standard derivation for both phantom A and phantom B. The scatter correction with our new scale factor proves to be an effective method for the 3D whole body PET scanner.

Table 3. Comparative studies of bias and standard derivation values of the results obtained from different scatter correction methods for phantom A. Test 1 is without scatter correction, test 2 is with scatter correction using a traditional scale factor from tail fitting, test 3 is with scatter correction using a scale factor including consideration of scatter events from outside the axial FOV, and test 4 is with scatter correction using a scale factor including consideration of scatter events from outside the axial FOV and multiple scatter events. The top one is for activity-free regions, the bottom one is for hot regions.

	test 1	test 2	test 3	test 4
bias	0.4903	0.2863	0.2278	0.0473
std	0.6817	0.4441	0.3791	0.1238
	test 1	test 2	test 3	test 4
bias	0.1577	0.1144	0.0989	0.0687
std	0.1871	0.1541	0.1439	0.1170

Table 4. Comparative studies of bias and standard derivation values of the results from different scatter correction methods for phantom B. Test 1 is without scatter correction, test 2 is with scatter correction using a traditional scale factor from tail fitting, test 3 is with scatter correction using a scale factor including consideration of scatter events from outside the axial FOV, and test 4 is with scatter correction using a scale factor including consideration of scatter events from outside the axial FOV and multiple scatter events. The top one is for activity-free regions, the bottom one is for hot regions.

	test 1	test 2	test 3	test 4
bias	8.145	3.187	2.358	0.774
std	20.201	7.763	5.661	1.940
	test 1	test 2	test 3	test 4
bias	0.6496	0.3715	0.3090	0.1324
std	0.7897	0.5200	0.4633	0.3218

4. Discussion and conclusion

We have developed and evaluated the scatter correction method based on SSS for our new PET scanner: Hamamatsu SHR74000. The programs introduce new components in the scale step for correcting scatter events from outside the axial FOV and multiple scatter events, especially concentrating on large objects. In a practical situation, the activity distributions outside the axial FOV are not uniform and it is not easy to get their accurate position information. Since the SHR74000 is also a PET/CT scanner, we hope that the accurate anatomic information provided by CT can help us to improve the scale factors. Experiments were performed to test the effects of scatter correction; the results show obvious improvements in the contrast of images, especially in the activity-free regions. The programs are proved to be effective in solving the case of large objects. Studies to obtain more accurate scale factors and experiments with more complicated phantoms and human bodies are underway.

Acknowledgments

We thank Hamamatsu Photonics K.K., for providing financial support and experimental conditions.

References

[1] Ollinger J M 1996 *Phys. Med. Biol.* **41** 153

[2] Watson C C 2000 *IEEE Trans. Nucl. Sci.* **NS-47**(4) 1587

[3] Watson C C 2007 *IEEE Trans. Nucl. Sci.* **NS-54**(5) 1679

[4] Accorsi R, Adam L E, Werner M E and Karp J S 2004 *Phys. Med. Biol.* **49** 2577

[5] Werling A, Bublitz O, Doll J, Adam L E and Brix G 2002 *Phys. Med. Biol.* **47** 2947

[6] Adam L E, Karp J S and Brix G 1999 *Phys. Med. Biol.* **44** 2879

[7] Thielemans K, Manjeshwar R M, Tsoumpas Ch and Jansen F P 2007 *A New Algorithm for Scaling of PET Scatter Estimates Using all Coincidence Events* Nuclear Science Symposium **M18** 338

[8] Jan S, Santin G and Strul D 2004 *Phys. Med. Biol.* **49** 4543

[9] Gao F, Yamada R, Watanabe M and Liu H F 2009 *Acta Phys. Sin.* **58** 712 (in Chinese)

[10] Markiewicz P J, Tamal M, Julyan P J, Hastings D L and Reader A J 2007 *Phys. Med. Biol.* **52** 829

[11] Gao F, Liu H F and Shi P C 2007 *Acta Phys. Sin.* **56** 4229 (in Chinese)